Advances in discrete element modeling of rock fracture for next-generation comminution models

Computational Particle Mechanics (2025) 12:4431–4449
https://doi.org/10.1007/s40571-025-01092-y

Advances in discrete element modeling of rock fracture for next-generation comminution models

Vedad Tojaga[1] · Mijo Nikolić[2] · Michael Denzel[3] · Jacinto Ulloa[4] · Adnan Ibrahimbegovic[5] · Magnus Evertsson[6] · Adam Bilock[7] · Timo Saksala[8] · Johannes Quist[1]

Received: 14 May 2025 / Revised: 15 August 2025 / Accepted: 23 October 2025 / Published online: 8 November 2025

Abstract

This paper provides a methodological overview of the current state of the art in discrete element modeling of rock fracture in the context of comminution, an energy-intensive process of breaking down rocks into smaller sizes. This process is essential for liberating valuable metals and minerals that are in growing demand for the green transition and the electrification of society. The paper covers the most recent developments and addresses fundamental issues in the bonded discrete element method, the lattice element method, the particle replacement method, and the level-set discrete element method. We argue that the most effective modeling approach must emerge from a synergy between solid mechanics, rock mechanics, and the comminution field—an effort made by this collaborating multidisciplinary group, with the goal of making the next generation of comminution models, powered by GPU-accelerated high-performance computing, more reflective of real-life rock behavior, advancing energy-efficient mining.

Keywords Comminution · Rock mechanics · Discrete element method (DEM) · Particle breakage · Mining · Fracture · GPU

1 Background and motivation

We need more metals and minerals for the green transition of our society. Around 2% of the world's global final energy consumption is consumed by the mining sector [1]. Of this, about 50% is consumed in the comminution[1] process of the ore, where the notoriously inefficient grinding processes are the largest single energy consumers, with reported energy efficiencies as low as 1% [3, 4], while crushing (see Fig. 1) is considerably more energy-efficient compared to conventional grinding [5, 6]. Such significant energy losses highlight the urgent need to improve the efficiency of comminution processes. By crushing more and grinding less, substantial amounts of energy can be saved. The typical particle size range for the processes considered spans from the meter scale down to the millimeter scale for crushing, while grinding typically handles particles from the millimeter scale down to the micrometer scale. In this context, it is also important to consider that ore grades are generally decreasing, since the most easily accessible ore deposits have already been exploited. As a result, larger quantities of fresh ore must be processed to produce the same amount of finished product. In addition, ore quality tends to be higher when mined from deeper levels of the earth. This is because deeper

✉ Vedad Tojaga
vedad.tojaga@fcc.chalmers.se

1 Department of Computational Engineering and Design, Fraunhofer-Chalmers Centre for Industrial Mathematics, Gothenburg, Sweden

2 Faculty of Civil Engineering, Architecture and Geodesy, University of Split, Split, Croatia

3 Swiss Tower Mills Minerals AG, Haselstrasse 1, 5400 Baden, Switzerland

4 Department of Mechanical Engineering, University of Michigan, Ann Arbor, MI, USA

5 Laboratoire de Mécanique, Université de Technologie de Compiègne - Alliance Sorbonne Université, Compiègne, France

6 Department of Industrial and Materials Science, Chalmers University of Technology, Gothenburg, Sweden

7 IPS Particle Technology AB, Gothenburg, Sweden

8 Faculty of Built Environment, Tampere University, Tampere, Finland

[1] The process of reducing the size of rocks, essential for liberating valuable minerals from the surrounding material. See, for example, a brief and recent YouTube video for visualization posted by the Sandvik Group [2].

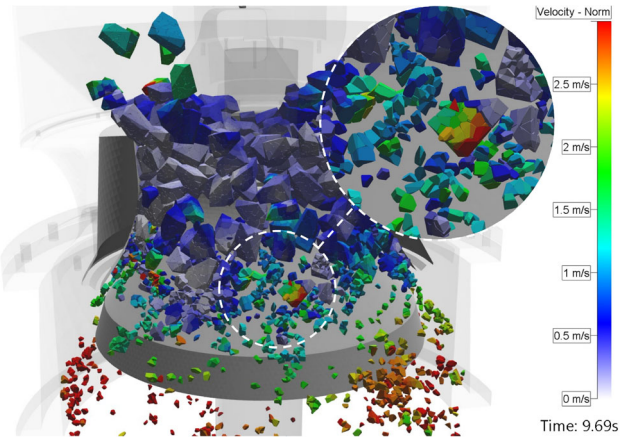

Fig. 1 Visualization of a DEM cone crusher simulation with resolved rock particle fracture, modified from [14]

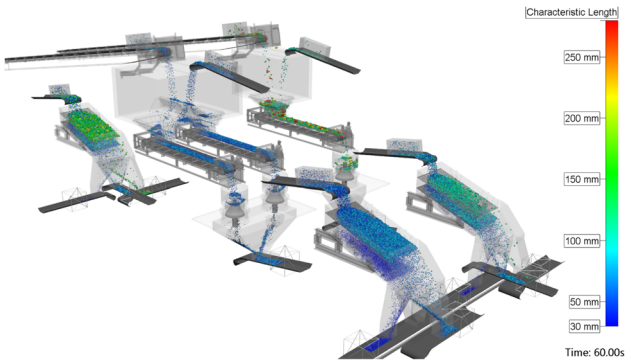

Fig. 2 A DEM simulation of a two-stage crushing and screening circuit begins with a primary screen feeding a secondary crushing and screening stage with recirculation, followed by a tertiary stage with a recirculating load from both the tertiary and secondary screens [15]

deposits are less affected by weathering processes, which can degrade ore quality over time. However, mining at greater depths demands significantly more energy than surface mining. Without technological advancements, sustaining current operations and meeting growing demand will likely lead to a significant increase in energy consumption, potentially rising by as much as a factor of 8 by 2060 [1]. In other words, sustainability begins with the materials extracted through mining.

To reduce energy consumption, new and optimized comminution equipment is of the utmost importance. A virtual comminution machine [7] facilitates the development of energy-efficient rock processing solutions, considering the significant costs and time involved in physical testing and field data modeling. In addition, it enables the identification of the optimal operation of existing comminution devices based on the mechanical properties of the ore. The discrete element method (DEM), developed by Cundall and Strack [8], is the preferred numerical method for modeling processes involving granular materials. The challenge in comminution modeling using DEM is twofold: (i) describing the mechanical behavior of rock and (ii) integrating it into an industrial machine-level simulation (see Fig. 1). This challenge was first identified in [9] and remains relevant today. Historically, the science of comminution has predominantly focused on the latter, whereas the rock and geomechanics research community has concentrated on the former. Advancements in the parallelization of DEM on graphics processing units (GPUs) using high-performance computing (HPC) have enabled efficient industrial-scale simulations and a more realistic representation of irregularly shaped particles in large systems (see Figs. 1 and 2) [10–14]. Complemented by material models from rock mechanics, we are now at a point where the research efforts of these two communities have the opportunity to converge.

This paper presents a methodological overview, with examples, of recent advances in discrete element modeling of rock particle breakage, followed by a discussion of future directions in comminution modeling. It offers a unique multidisciplinary perspective, incorporating insights from solid mechanics, rock mechanics, and the comminution field—a perspective needed for redefining the next generation of comminution models by leveraging the new computing capabilities available today. Rather than providing a fully comprehensive review of particle breakage [16], we focus on fundamental issues related to particle breakage using DEM in the context of comminution and how this collaborative group is addressing these challenges. The methodological review does not include empirical or machine learning-based comminution models, but fully physics-based ones. Some recent examples of the former are provided in [17–19]. Another active research field is FEM–DEM coupling strategies [20–25]; however, due to their added computational cost in describing the mechanical response of rock, they have yet to be applied to the field of comminution.

2 An overview of the discrete element method

In DEM, the movement of the particles is governed by contact mechanics and Newton's second law of motion, i.e.,

$$m_i \frac{d^2\mathbf{x}_i}{dt^2} = \mathbf{F}_i, \tag{1}$$

$$\mathbf{I}_i \frac{d^2\Theta_i}{dt^2} = \mathbf{M}_i, \tag{2}$$

where, for particle i, m_i is the mass, $\mathbf{I}_i$ is the second-order moment of inertia tensor, $\mathbf{x}_i$ and Θ_i are the position of the center of mass and the orientation, respectively, and $\mathbf{F}_i$ and $\mathbf{M}_i$ are the acting force and moment, respectively. The ordinary

differential equations (ODE) can be solved using explicit time integration schemes such as forward Euler, e.g.,

$$\ddot{\mathbf{x}}_i(t) = \frac{\mathbf{F}_i(t)}{m_i}, \tag{3}$$

$$\dot{\mathbf{x}}_i(t + \Delta t) = \dot{\mathbf{x}}_i(t) + \ddot{\mathbf{x}}_i(t)\Delta t, \tag{4}$$

$$\mathbf{x}_i(t + \Delta t) = \mathbf{x}_i(t) + \dot{\mathbf{x}}_i(t)\Delta t, \tag{5}$$

where t is the time, $\dot{(\,)} = \frac{d(\,)}{dt}$, and $\ddot{(\,)} = \frac{d^2(\,)}{dt^2}$. Alternatively, the widely used velocity Verlet algorithm, leapfrog integration, and similar methods can be applied. To avoid the computationally expensive matrix inversion in Eq. (2) during numerical integration, it is advantageous to use an eigendecomposition of the inertia tensor. Since the inertia tensor is a real and symmetric matrix, it always results in a diagonal tensor in the particle body frame. Additionally, time integration of Newton's second law for rotation using quaternions is a robust method that avoids the issues of singularities with Euler angles [26].

The particles may overlap as long as the overlap distance is significantly smaller than the particle size, ensuring negligible deformation and thus particle (pseudo-)rigidity. In principle, any contact model can be used to compute forces from particle penetrations. However, a Hertz-type model is among the most commonly used, despite the fact that Hertz contact theory is only physically correct for spherical particles with linear elastic material behavior and small deformations at the point of contact [27].

In DEM, two fundamentally different approaches to particle breakage modeling have emerged [9, 16, 28], each with its own advantages and disadvantages. The first approach involves replacing a particle with smaller fragments or particles, while the second approach involves removing a bond in a bonded particle model or glued particle assembly. The second approach will be addressed first, as it dates back to the 1980 s and the lattice models of rocks, followed by the first.

3 Recent advances in discrete element modeling of particle breakage

3.1 Bonded discrete element method

A rock can be viewed as an assembly of glued particles, where each particle represents a grain, and the glue represents the matrix (cement) holding the grains together. Perhaps the most well-known variant of DEM that treats rocks accordingly is the bonded particle model by Potyondy and Cundall [29], which is implemented in major commercial DEM software packages such as EDEM by Altair, LS-Dyna by Ansys, and PFC by the Itasca Consulting Group. This

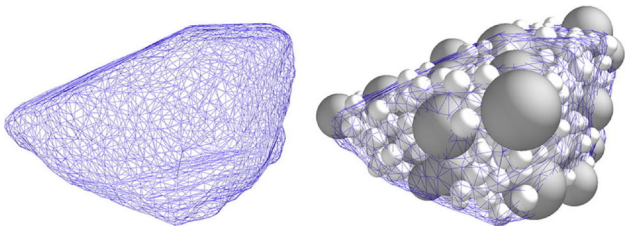

Fig. 3 Illustration of a cluster of packed spheres, selected from a 3D laser scan of a rock, suitable for use with the Potyondy and Cundall bonded particle model of rock [32]. The virtual bond beams are connecting the centers of the spheres. For reference, the particle size distribution of the feed is shown in [32]

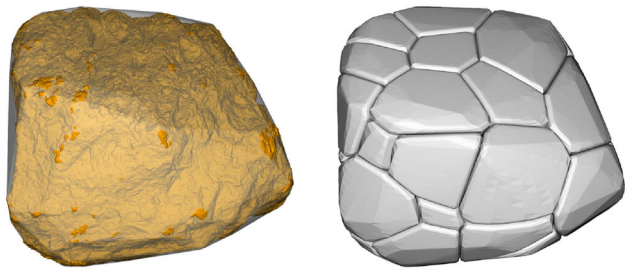

Fig. 4 Illustration of a cluster of tightly packed Voronoi cells, selected from a 3D laser scan of a rock, suitable for use with the bonded Voronoi cell model of rock [14]. The virtual bond springs are connecting the nodes of the polyhedra. For reference, the maximum distance between any two points within the volume measures 65.5 mm

widespread implementation makes it easily accessible for use in both research and industry [30–33]. In this model, spherical particles are connected by virtual Timoshenko beams as illustrated in Fig. 3. When the maximum tensile or shear stress within a beam exceeds its tensile or shear strength, the beam is removed, leaving a contact model between the now-disconnected particles. In addition to inter-granular fracture, intra-granular fracture can be represented using clusters of bonded particles, indicating that grain failure is possible. Grain boundaries are modeled as weaker bonds with Weibull-distributed strengths [34–36].

Voronoi cells, as illustrated in Fig. 4, are often preferred over spherical particles because they can be bonded along their faces, preserving volume during the fragmentation process, among other advantages [37–39]. Additional advantages of using Voronoi cells over spheres include their closer resemblance to the irregular, polyhedral shapes of natural grains, their ability to achieve higher packing densities, and the ease of incorporating varying grain sizes and heterogeneity into the bonded cell model (see Figs. 3 and 4 for comparison). Moreover, Voronoi cells produce more realistic and complex fracture patterns along grain boundaries or weak planes. Although their complex shapes may introduce some computational overhead, Voronoi cells can be more efficient overall by reducing the need for excessively fine discretizations, as shown in Figs. 3 and 4.

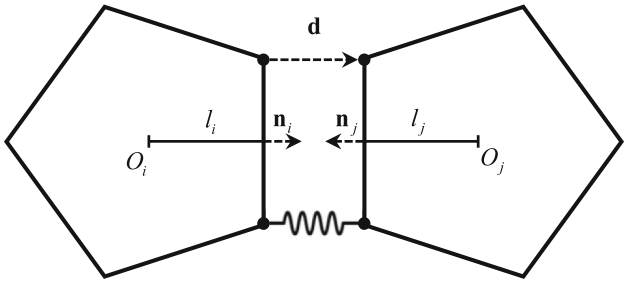

Fig. 5 Illustration of nodally bonded cell model

Whether the bonded cell model or the bonded particle model is used, a recurring issue with the application of the bonded discrete element method in the literature is mesh objectivity [40]. This issue is illustrated through a simple analytical example presented in the next section, followed by an extended review of some of the latest solutions from the computational mechanics research community.

3.1.1 The consequence of the brittle fracture assumption

A displacement vector $\mathbf{d}$ connecting two bonded points is considered in Fig. 5. The unit normal vector to the surface of the bond can be defined as

$$\mathbf{n} = \frac{\mathbf{n}_i - \mathbf{n}_j}{|\mathbf{n}_i - \mathbf{n}_j|}, \tag{6}$$

where $\mathbf{n}_i$ is the outward normal to the surface of one particle, and $\mathbf{n}_j$ is the outward normal to the surface of the other particle. To calculate the normal strain ε in the bond, the reference length $l = l_i + l_j$ is introduced, defined as the sum of the distances from the center of each particle to the interface. The normal strain ε is then the projection of the displacement vector $\mathbf{d}$ in the direction of the bond's surface normal $\mathbf{n}$, normalized by the reference length l, i.e.,

$$\varepsilon = \frac{\mathbf{d} \cdot \mathbf{n}}{l}. \tag{7}$$

From the additive decomposition of $\mathbf{d}$ into the normal direction $\mathbf{n}$ and the tangential direction

$$\mathbf{t} = \frac{\mathbf{d} - (\mathbf{d} \cdot \mathbf{n})\mathbf{n}}{|\mathbf{d} - (\mathbf{d} \cdot \mathbf{n})\mathbf{n}|}, \tag{8}$$

the engineering shear strain in the bond can be obtained as:

$$\gamma = \frac{|\mathbf{d} - (\mathbf{d} \cdot \mathbf{n})\mathbf{n}|}{l}. \tag{9}$$

The normal stress and shear stress in the bond, $\sigma = k_n \varepsilon$ and $\tau = k_t \gamma$, respectively, can be calculated using a constitutive relationship, such as Hooke's law, where k_n and k_t represent the normal and tangential material stiffness, respectively. An upper limit, the material strength, is introduced for the normal and shear stress, denoted as $\bar{\sigma}$ and $\bar{\tau}$, respectively. A wide range of failure criteria can be applied here depending on the load case, such as Rankine's theory, Mohr–Coulomb, Drucker–Prager [41]. For the sake of simplicity, an uncoupled failure criterion is considered, e.g., $\sigma = \bar{\sigma}$. The energy needed to break the bond in tension is defined as the area beneath the force–displacement curve and is commonly referred to as the mode I fracture energy, denoted as G_I. The physical area allocated to each bond, A/n, is the interface area A divided by the number of bonds n. In the case of sudden bond removal in tension once the normal stress σ reaches the tensile strength $\bar{\sigma}$, the fracture energy G_I is the area beneath a right triangle with a fixed height $\bar{\sigma} A/n$ and a width, or displacement at failure initiation, $u_0 = \bar{\sigma} l / k_n$ (see Fig. 6), i.e.,

$$G_I = \frac{\bar{\sigma}^2 A l}{2 n k_n}. \tag{10}$$

Note that the fracture energy G_I is size-dependent because the displacement at failure initiation u_0 is a function of the reference length l. That is, for a given particle–particle pair size, a unique fracture energy is defined, leading to a lack of mesh objectivity for the discretized rock. In other words, since the size of the rock is constant until fracture, the bond material connecting the sub-particles should have the same material properties regardless of the size of the bonds. Additionally, as $l \to 0$, $G_I \to 0$, a physically meaningless result because the stored elastic energy is dissipated through crack propagation, sound and heat generation, and the kinetic energy of the broken pieces.

In the specific case of the classical bonded particle model in Fig. 3, arbitrary size-dependent fracture energies are assigned to the same homogeneous bond material. As a result, the simulation results will not converge with continuous mesh refinement. Consequently, what is known as fracture energy regularization is needed. This phenomenon is well understood in the research field of the finite element method (FEM), but it also applies to DEM, though it is rarely addressed—except in a more recent work [40], to the authors' knowledge. This observation is also emphasized by the widespread use of the brittle fracture criterion in the DEM literature, facilitated by open-source software packages [42–44], as well as the previously mentioned commercial software.

In the next two sections, two common types of fracture energy regularization are presented: the simplest, based on linear softening, and the more advanced strong discontinuity approach. While the latter has yet to be adopted in the field of DEM, it can be integrated, as demonstrated below.

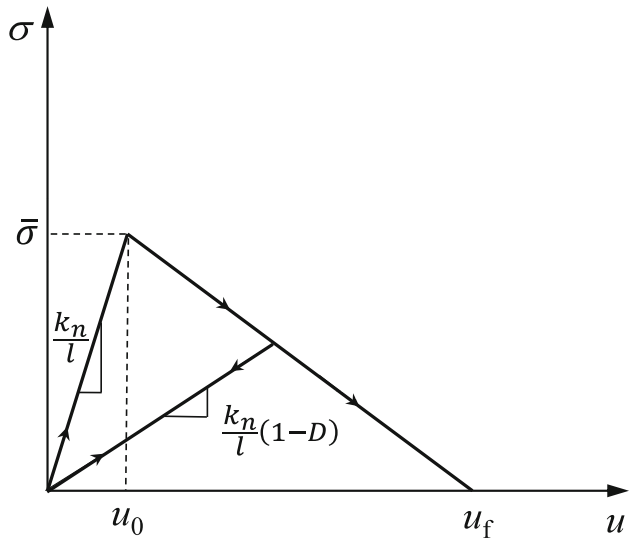

Fig. 6 Bi-linear cohesive traction-separation law

3.1.2 Fracture energy regularization

In the previous section, it was demonstrated that the brittle fracture criterion commonly used in bonded discrete element modeling of rock fracture lacks mesh objectivity and therefore requires regularization of the problem. The simplest fracture energy regularization technique is based on a linear softening traction-separation law (Fig. 6). When the normal stress σ reaches the tensile strength $\bar{\sigma}$, failure initiates at the displacement u_0. Note that the displacement at failure initiation u_0 varies with the slope of the linear force–displacement curve, given by k_n/l, while the peak force remains constant at $\bar{\sigma}\,A/n$. Instead of abrupt rupture, the damage progresses according to linear softening until the normal stress σ reaches zero at full rupture. In this case, the displacement at full rupture u_f is determined by the area under the force–displacement curve G_I and the peak force $\bar{\sigma}\,A/n$ as follows:

$$u_\mathrm{f} = \frac{2G_I n}{\bar{\sigma}\,A}. \tag{11}$$

This approach eliminates the dependency on the reference length l, ensuring a consistent fracture energy across all mesh discretizations. Although the displacement at full rupture u_f is defined in Eq. (11), the slope of the softening force–displacement curve varies with the reference length l, while the area under the entire force–displacement curve G_I remains constant. This behavior is similar to the mesh-dependent softening modulus [45] and the cohesive zone model [16, 46–48].

The transition zone between failure initiation and full rupture can be modeled using classical continuum damage mechanics. To describe the evolution of damage in the bond, an irreversible Kachanov-like damage variable $D \in [0, 1]$ is introduced, where $D = 1$ represents a fully damaged bond and $D = 0$ represents an undamaged bond. Linear softening can be expressed as follows:

$$D = \frac{u_\mathrm{f}\,(u_\mathrm{max} - u_0)}{u_\mathrm{max}\,(u_\mathrm{f} - u_0)}, \tag{12}$$

where u_max represents the maximum attained displacement value in the loading history. The force (and stiffness) is then gradually reduced by a factor of $(1 - D)$, i.e., $(1 - D)\sigma A/n$ (see Fig. 6).

For mixed-mode fracture, it is useful to introduce the magnitudes of the Cauchy traction vector $\mathbf{T} = \sigma\mathbf{n} + \tau\mathbf{t}$ and the displacement vector $\mathbf{d}$, and to redefine the previously mentioned expressions in terms of these effective quantities [47, 49]. Consequently, the fracture energy is considered as an effective measure rather than a real one.

While it is straightforward to relate the fracture energy to the displacement at full rupture analytically for linear softening, this process becomes more cumbersome with an exponential degradation function [40, 50]. This can lead to the problem of assigning an arbitrary size-dependent fracture energy to the same bond material if the displacement at full rupture remains constant and heterogeneous particle size distributions are considered in bonded models. Therefore, it is important to explicitly specify the fracture energy in such cases, particularly because an exponential degradation function is often necessary in bonded discrete element modeling to accurately capture the entire force–displacement curve observed in experimental tests [40, 50], especially given the heterogeneous size distribution of natural rock grains. In the next section, an elegant solution to this problem is presented using the strong discontinuity approach, which also incorporates a physical fracture process zone within the bond. Emphasis is placed on the adaption of the theory for use in DEM.

3.1.3 Strong discontinuity approach adapted to the bonded discrete element method

Cracks are characterized as locations exhibiting a distinct discontinuity or abrupt change in the displacement field, resulting in different movements between one side of the crack and the other. To express this concept mathematically, it is appropriate to additively split the displacement, e.g., the normal displacement $u = \mathbf{d} \cdot \mathbf{n}$, into a regular part, $\bar{u}$, and a crack opening displacement jump, α, utilizing the Heaviside step function, H [51], i.e.,

$$u = \bar{u} + H\alpha, \tag{13}$$

where

$$H = H(x) = \begin{cases} 1 & \text{if } x \geq x_c, \\ 0 & \text{if } x < x_c, \end{cases} \tag{14}$$

and $x = x_c$ represents the bonded point along the reference length of the bond l in Fig. 5. In Eq. (13), we may add and subtract the jump variable α multiplied by a continuous function $N = N(x) = x/l$, i.e.,

$$u = \underbrace{\bar{u} + N\alpha}_{\hat{u}} + (H - N)\,\alpha. \tag{15}$$

This rewriting will facilitate the calculation of the displacement jump [52].

Upon differentiation of Eq. (15) with respect to x, the strain is obtained as

$$\varepsilon = \hat{\varepsilon} + G\alpha + \delta(x - x_c)\alpha, \tag{16}$$

where $G = -1/l$ and

$$\delta(x - x_c) = \begin{cases} \infty & \text{if } x = x_c, \\ 0 & \text{if } x \neq x_c, \end{cases} \tag{17}$$

is the Dirac delta function. Note that the first term in Eq. (16) explicitly reads $\hat{\varepsilon} = d\hat{u}/dx = (\bar{u} + \alpha)/l$, and the first two terms in Eq. (16) represent the deformation in the bulk material at $x \neq x_c$, while the last term can be viewed as the deformation associated with the discontinuity at $x = x_c$.

It is necessary to formulate the internal virtual work of the bond to arrive at the governing equilibrium equation to be solved. The work done by the internal force (stress σ) within the bond during a virtual displacement, denoted as δu, is defined as the internal virtual work. Virtual displacements are hypothetical, small changes in the displacement field of the bond that satisfy the boundary conditions (i.e., they are kinematically admissible). These displacements induce virtual strains, $\delta\varepsilon$. The internal virtual work for the bond takes the form

$$\int_0^l \delta\varepsilon\,\sigma\,dx = \int_0^l \frac{d\delta\hat{u}}{dx}\sigma\,dx + \delta\alpha\int_0^l [\delta(x - x_c) + G]\,\sigma\,dx. \tag{18}$$

The second term in Eq. (18) represents the enhanced contribution to the internal virtual work from the strong discontinuity. To satisfy stress equilibrium, this term must be zero for all admissible variations of $\delta\alpha$, yielding the governing equilibrium equation

$$\int_0^l [\delta(x - x_c) + G]\,\sigma\,dx = 0 \implies \sigma(x_c) - \sigma = 0, \tag{19}$$

where σ represents the stress in the bulk material, while

$$\sigma(x_c) = \int_0^l \delta(x - x_c)\sigma\,dx$$

represents the stress at the discontinuity, $x = x_c$, using the fundamental property of the Dirac delta function. Equation (19) ensures a state of equilibrium within the bond. Compared to the fracture energy regularization based on linear softening, an infinitesimal physical length scale is present in the neighborhood of $x = x_c$, similar to a cohesive fracture description. Note that the exact position of the discontinuity at $x = x_c$ does not need to be explicitly specified in the presented framework when applied to the bonded discrete element method, as it is inherent in the equilibrium equation (19). Moreover, as shown next, it does not need to be considered in the computation of the displacement jump or strain, along with the Dirac delta function (17).

The calculation steps to evaluate the displacement jump α iteratively are based on the framework of computational inelasticity, where the displacement jump α is essentially treated as the plastic strain (cf. Fig. 7). To illustrate this, a yield criterion of the type

$$\phi = \sigma - [\bar{\sigma} + q] = 0 \tag{20}$$

is considered. Here, q, which is initially zero, is a stress-like variable that ensures the material weakens when loading exceeds the material strength threshold $\bar{\sigma}$. Equation (20) can be interpreted as the equilibrium equation (19), where the first term represents the stress in the bulk material, i.e., $\sigma = k_n\hat{\varepsilon} + G\alpha$, and the bracketed term is associated with the stress at the discontinuity, with q representing a negative stress increment. In the case of linear softening, q takes the form

$$q = k_s\beta, \tag{21}$$

where $k_s < 0$ is the softening modulus, and $\beta \geq 0$ is an internal softening variable, resembling an internal hardening variable in plasticity. The displacement jump α is updated along with the internal softening variable β, similar to the plastic strain and the internal hardening variable in linear plasticity, following a return-mapping algorithm explained in detail elsewhere [45, 53, 54].

The area under the linear traction-separation law, i.e., the σ-α curve, denoted as G_I^*, can be expressed in terms of the softening modulus k_s and the material strength $\bar{\sigma}$ as follows:

$$G_I^* = \frac{\bar{\sigma}^2}{2\,|k_s|}, \tag{22}$$

and related to the fracture energy G_I via the cross-sectional area of the bond, i.e., $G_I = G_I^* A/n$. The maximum attain-

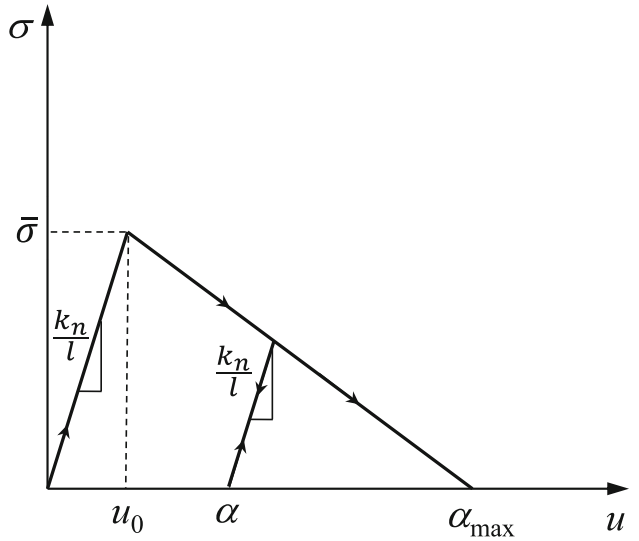

Fig. 7 Bi-linear cohesive traction-separation law based on the strong discontinuity approach

able displacement jump at full rupture is then given by $\alpha_{\max} = 2G_I^*/\bar{\sigma}$.

In the case of exponential softening, the stress-like variable q takes the form:

$$q = -\bar{\sigma}\left[1 - \exp\left(-\frac{\bar{\sigma}}{G_I^*}\beta\right)\right]. \tag{23}$$

The softening modulus k_s can then be derived from Eq. (23) as $k_s = \frac{dq}{d\beta}$. Note that for a nonlinear softening law, the softening modulus $k_s = k_s(\beta)$ is an additional unknown. Consequently, the solution procedure requires a nested Newton–Raphson method to determine the value of the internal softening variable β that satisfies the equilibrium equation before updating the displacement jump α, among other variables [55]. This approach is also common in nonlinear elastoplasticity.

Unlike the fracture energy regularization based on linear softening, which relies on classical continuum damage mechanics, the strong discontinuity approach ensures crack irreversibility through the displacement jump α (see Fig. 7), similar to the plastic deformation in plasticity theory. Moreover, the strong discontinuity approach incorporates a physical fracture process zone within the bond material. Finally, the energy required to break the bond can be easily integrated into the strong discontinuity approach, regardless of whether linear or exponential softening is considered.

3.1.4 Accounting for loading rate dependency

Rock materials exhibit strong sensitivity to loading rate, which, as the rate increases, manifests as strain rate hardening and a transition from a single crack to multiple crack/fragmentation failure modes [56]. Moreover, the sensitivity to loading rate shows a two-phase behavior such that, under compression, the dynamic increase factor (DIF)—the ratio of dynamic strength to quasi-static strength—remains linear up to a strain rate of approximately 10^1, after which the DIF increases exponentially. Since such strain rates can be easily reached in comminution machines [57], it is important to account for loading rate dependency in the model. This can be achieved in analogy to extending traditional elastoplasticity to viscoplasticity [58]. We illustrate this approach by adding a linear viscosity term to the 1D strong discontinuity model described above in Sect. 3.1.3.

We choose the consistent viscoplasticity approach proposed by Wang et al. [59] for this purpose, because, unlike the Perzyna and Duvaut–Lions-type overstress models, it restores the consistency condition (i.e., the stress state remains on the yield surface during plastic flow), thereby enabling the use of robust methods from computational rate-independent plasticity for stress integration, such as return mapping [60]. In this setting, the yield criterion from the previous section now reads

$$\phi_d = \sigma - \left[\bar{\sigma} + q(\beta, \dot{\beta})\right] = 0, \tag{24}$$

$$q = k_s\beta + s_d\dot{\beta}, \tag{25}$$

$$\phi_d \leq 0, \quad \dot{\beta} \geq 0, \quad \phi_d\dot{\beta} = 0, \tag{26}$$

where ϕ_d is the rate-dependent loading function, s_d is the (non-negative) viscosity modulus, and $\dot{\beta}$ is the rate of change of the internal softening variable. Moreover, Eq. (26) represents the classical loading/unloading conditions of rate-independent plasticity.

A note on stress integration is necessary here. Specifically, when using the consistency condition, i.e., $\dot{\phi}_d = 0$, to derive the relation for the viscoplastic increment, i.e., $\dot{\beta}$, its second time-derivative appears in the expression. However, this complication can be avoided in the algorithmic treatment of the consistency condition by replacing $\dot{\beta}$ with its algorithmic counterpart, $\dot{\beta} \approx \Delta\beta/\Delta t$. In this way, the stress integration can be performed in a manner similar to that in rate-independent models. Further details can be found in [59].

The identification of the constant viscosity modulus, s_d, is carried out based on uniaxial experimental data. It being a constant means that it must be re-identified if the loading rate changes significantly. Alternatively, it can be replaced by a strain rate-dependent modulus, which, however, introduces an additional nonlinearity to the model. The effect of the viscosity modulus is illustrated in Fig. 8.

When the viscosity modulus differs from zero, the model exhibits higher stress and more ductile behavior. Moreover, there is always some residual stress, which can, however, be eliminated using special techniques. Additionally, a similar effect is achieved when the viscosity modulus is kept constant

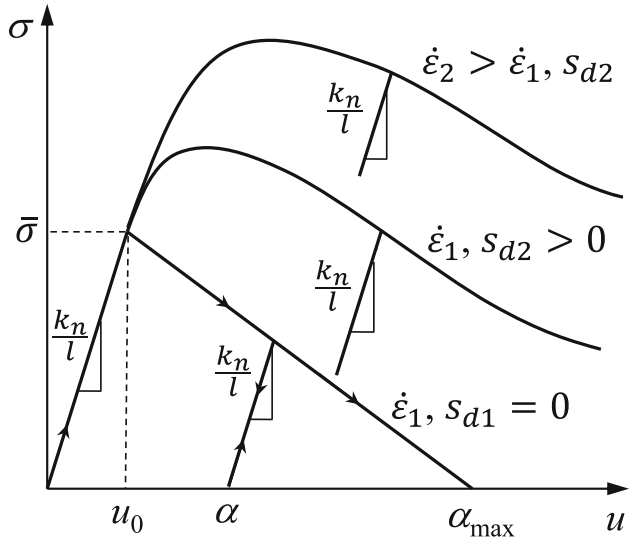

Fig. 8 Rate-dependent cohesive traction separation law based on the strong discontinuity approach. Here, $\dot{\varepsilon}_1$ is a strain rate; s_{d1} is the nonzero viscosity modulus at the strain rate $\dot{\varepsilon}_1$ (i.e., the quasi-static case); s_{d2} is a viscosity modulus greater than zero (i.e., the rate-dependent case); and $\dot{\varepsilon}_2$ is a strain rate higher than $\dot{\varepsilon}_1$

but the strain rate is increased. Finally, the fracture energy, which also increases upon increasing strain-rate [56], can be made rate-dependent simply by replacing $\bar{\sigma}$ in Eq. (22) with $\bar{\sigma} + s_d^* \dot{\beta}$, where s_d^* is another viscosity modulus requiring identification based on experiments.

3.1.5 Lattice element method

The lattice element method (LEM) shares similarities with the bonded discrete element method but has a key distinction: it typically preserves element connectivity without overlap between particles, as seen in DEM (see, e.g., [49, 61–64]). As a result, LEM is primarily utilized for crack propagation and failure analysis of concrete [65, 66] and rocks [67, 68] under quasi-static loading conditions, though dynamic-induced failure and crack propagation can also be considered [49, 55, 69]. LEM therefore primarily employs implicit finite element solution methods, unlike the explicit methods used in DEM. The goal of LEM is to accurately capture post-peak softening behavior, dissipated energy, and failure associated with propagating cracks.

Similar to the bonded cell model, LEM often represents rigid particles using Voronoi cells, which form an assembly to simulate the material domain (see Fig. 9). These particles are connected by cohesive links (lattice elements), modeled using one-dimensional mechanical components such as truss bars, beams, or springs. Under loading, certain elements fail when their stress or strain exceeds specified thresholds, leading to the formation of dominant cracks as neighboring elements subsequently fail.

In LEM, various models exist for representing the mechanics of lattice elements between Voronoi cells, each offering different mechanisms for force and moment transmission. Truss bar-based models can carry only axial forces within the bond. Rigid body spring models use normal, shear, and rotational springs to represent bond mechanics. Additionally, lattice discrete particle models have been developed to carry both normal and shear forces in the bond [64]. Euler–Bernoulli beam models can transmit axial forces and bending moments but do not account for shear deformations, limiting their applicability in scenarios where shear effects are not significant. In contrast, Timoshenko beam models offer an improved approach by incorporating both bending moments and shear deformations, along with axial forces. Depending on the chosen model, the kinematics of lattice elements can include normal and engineering shear strain, as in Eqs. (6) and (7) of the bonded discrete element method, as well as rotations of the lattice elements.

The classical LEM also suffers from mesh objectivity issues when representing discontinuous failures. Various approaches have been proposed to regularize this problem (see [63]). One common remedy involves a regularized linear softening traction-separation law, as described in Sect. 3.1.2. Alternatively, the softening behavior can be regularized using exponential softening through the application of strong discontinuities, as presented in Sect. 3.1.3. The incorporation of strong discontinuities into the LEM has been explored in recent works [63, 69, 70]. This regularization technique is effective in both quasi-static and dynamic versions of the method, resulting in a mesh-independent energy dissipation during material failure. Figure 10 illustrates dynamic crack propagation using the LEM method enhanced with strong discontinuities. The test, conducted using the Kalthoff experiment across different mesh sizes, demonstrated that the energy dissipation during fracture remains consistent across all mesh sizes [69].

More recent lattice elements include geometrically nonlinear Reissner beams with embedded strong discontinuities to account for large rotations of detached neighboring particles [71, 72], which are highly relevant in the bonded discrete element method, as first pointed out in [49] (see, e.g., Figs. 1 and 2 elsewhere [71]). Cosserat rods have also been recently applied to the bonded discrete element method [73].

3.1.6 Summary

In the bonded discrete element method, a rock can be treated as an assembly of irregularly shaped particles held together by cohesive lattice elements. This model representation allows for the description of inter- and intra-granular fracture, which is particularly useful for comminution, enabling the prediction of the product size distribution. However, the classical bonded discrete element method suffers from mesh

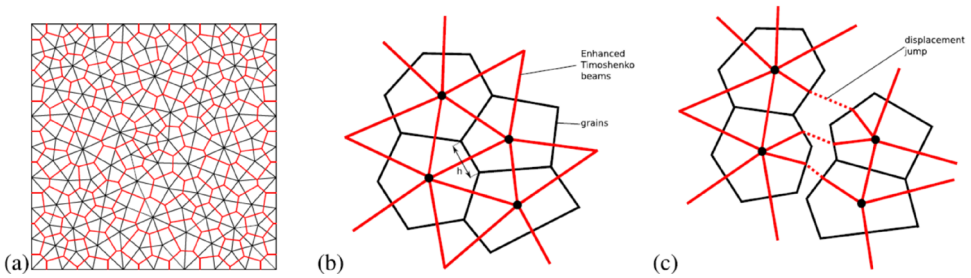

Fig. 9 Lattice element method: **a** Structure of the discrete lattice model with Voronoi cells as units of material and cohesive links modeled as enhanced Timoshenko beams between them; **b** neighboring Voronoi cells, where h is extracted from the Voronoi diagram and represents the height of the beam cross-section; **c** failure of adjacent cohesive links as the crack propagation mechanism (Figure from [69])

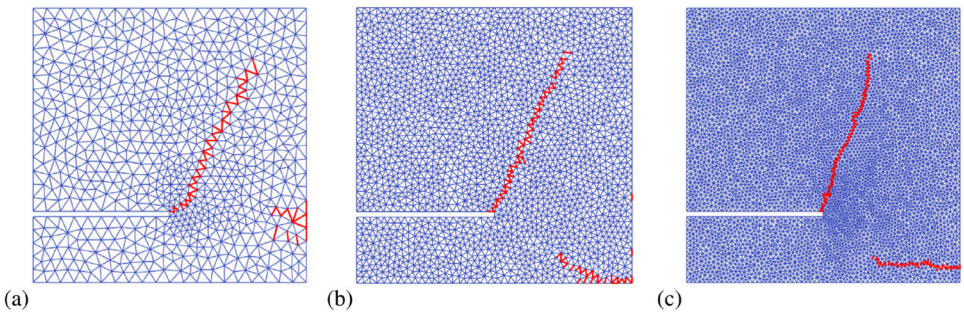

Fig. 10 Dynamic propagation test (Kalthoff): crack opening at the end of simulation time using the discrete lattice model for **a** 2122 elements, **b** 6732 elements, and **c** 17,629 elements; the applied impact velocity is $v_0 = 16.5$ m/s. More details can be found in [69]

objectivity issues when representing discontinuous failures. In addition, it is rate-independent, whereas rock materials exhibit strong sensitivity to the loading rate, leading to strain-rate hardening and a transition from single-crack to multiple-crack/fragmentation failure modes. These two fundamental issues are addressed in Sect. 3.1, where we utilize the cohesive zone model, the strong discontinuity approach, and the theory of viscoplasticity.

3.2 Particle replacement method

In the particle replacement method [74–76], particles are instantaneously replaced by several smaller progeny particles within the volume domain of the mother particle when a failure criterion is met (see Fig. 11). Here, "instantaneously" refers to the replacement occurring within a single time step. The progeny particles can assume various shapes, such as spheres or clumped spheres [77–81], superquadrics [82], or polyhedral particles [83, 84]. As another example, a model implemented in Ansys Rocky DEM, based on the breakage description by Tavares [85], uses the Voronoi subdivision algorithm to ensure mass and volume conservation [86]. This approach was validated through single particle drop weight tests [87]. Additionally, breakage tests were simulated using polyhedral particles and Voronoi tessellation [83]. Although spherical mother particles are typically used for simplicity, alternative shapes can also be considered. The failure criterion in such models could be, for instance, the exceedance of a critical force or energy threshold. One significant advantage of the replacement method is its ability to define the sizes of the progeny particles, allowing for the specification of any desired fragment size distribution. Another benefit is that, unlike other breakage models such as the bonded particle model, the replacement approach does not require additional calibration. This method has been effectively used to describe particle breakage under confined conditions [77, 88] and in comminution equipment, including various types of crushers [79, 82, 89, 90]. However, the particle replacement method struggles to accurately capture the force–displacement response, a limitation addressed more effectively by the bonded particle model [91].

The vast majority of particle replacement models use spheres as progeny particles due to their computational efficiency. However, a major disadvantage of this approach is the volume loss that occurs when a large sphere is replaced by several smaller, embedded spheres. To ensure mass constancy, a compensation approach involving the adjustment of fragment density was proposed in [93]. While this adjustment is often negligible in applications such as mills and crushers, where flow behavior is of lesser importance, it is less suitable for conveying processes, as the altered density distorts flow behavior and affects the loads on conveying equipment. In the work by Tavares and das Chagas [92], the constancy of volume and mass is maintained by overlapping smaller embedded spheres and defining damping factors for subsequent time steps to prevent instability or "explosions." Despite these advancements, spherical particles have inherent limitations, including their inability to accurately

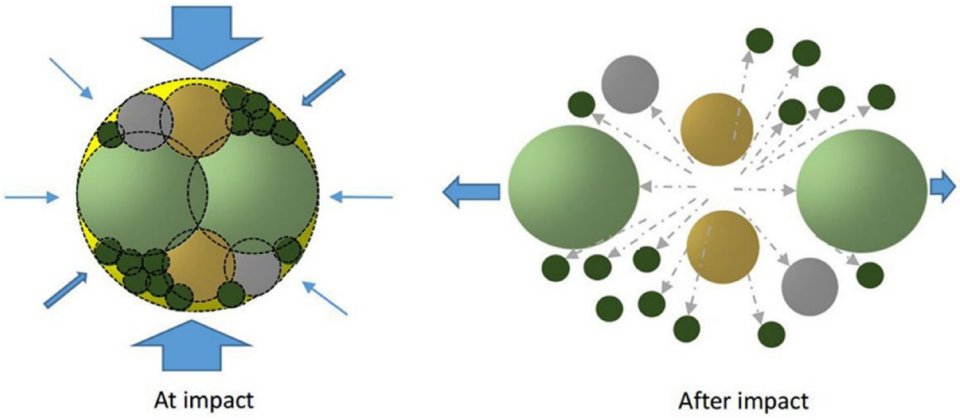

Fig. 11 Particle replacement with smaller spherical progeny particles within the volume domain of the mother particle [92]

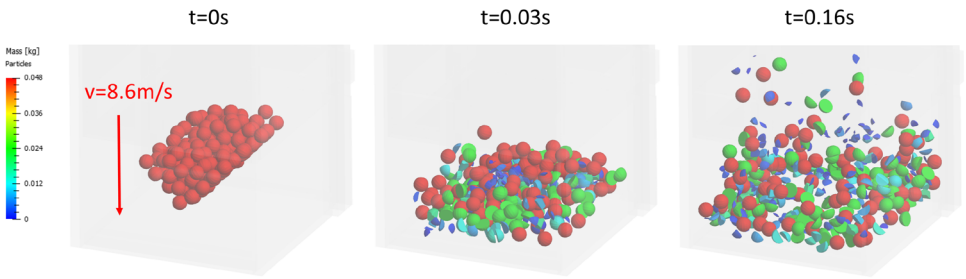

Fig. 12 Breakage simulation of a shattering test using the model in [95]: a probabilistic particle replacement with Voronoi fragments

represent particle shapes and their unsuitability for applications involving multiple breakages or further crushing of fragments—issues that are better addressed using polyhedral particles. On the other hand, the use of spherical particles offers distinct advantages in terms of computational efficiency. With spherical particles, contact detection and force calculations require minimal effort, and converting to any specific size distribution is straightforward [94].

3.2.1 Probabilistic particle replacement with Voronoi fragments

A recent probabilistic method proposed in [95, 96] builds upon the general framework introduced in [92], with significant differences in particle shape and the critical condition for failure. This model employs polyhedral particles, which are probabilistically replaced with Voronoi-tessellated breakage patterns when a critical mass-specific breakage energy threshold is exceeded. Initially presented in [97–99] and detailed in [96], the model facilitates the simulation of particle breakage within the DEM framework, including multiple breakage events and further fragmentation of resulting fragments. Validation of the model was conducted through shatter tests (see Fig. 12), as described in [95, 97], with calibration performed using a highly automated single particle impact tester [100]. The model is capable of efficiently simulating various processes—such as conveying [97, 101], mixing [102–104], and comminution—to predict the resulting particle size distribution with high accuracy.

For Voronoi tessellation, polyhedral particles are necessary. In this model, the initial particles are nearly spherical (see Fig. 13), although they can be of any convex shape, allowing the capture of irregularly shaped rocks. Depending on the stress state, the initial particles are probabilistically replaced by various particle shapes, following a method similar to that described in [81, 92]. However, unlike the approach by Tavares et al. [92] and related works, the initial particle is replaced with distinct breakage patterns rather than smaller spheres, ensuring conservation of both mass and volume. These breakage patterns are replicas of the initial particle that have been pre-tessellated using the Voronoi algorithm (see Fig. 13). Replacing particles with predefined breakage patterns is computationally more efficient than tessellating the particle at the moment of breakage, which would require executing the Voronoi algorithm for every breakage event. In the initial version of this model, progeny particles inherit the same velocities as the mother particle; however, this can be modified. Generally, energy dissipation during breakage and the distribution of fragment velocities are considered key data in breakage simulations. In scenarios involving complex loading, the highest force often determines failure, though other failure conditions may also be defined.

3.2.2 Single-particle breakage tests

Single-particle breakage tests aim to obtain the product size distribution resulting from the application of energy through experiments that replicate real-world conditions in a labo-

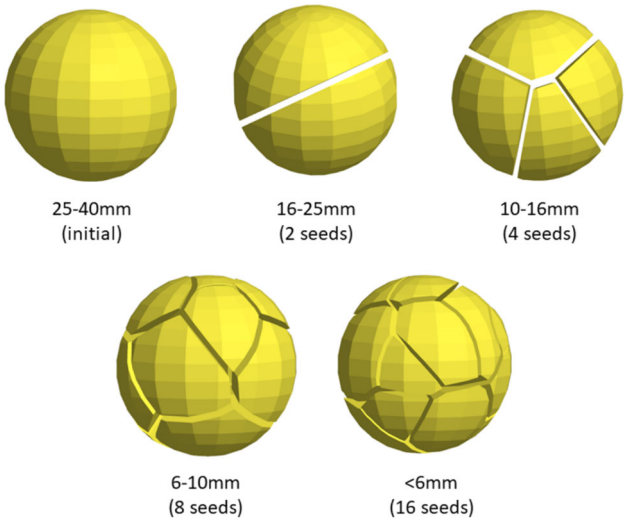

Fig. 13 Breakage patterns, which are Voronoi-tessellated polyhedral particles [97]

ratory setting. For example, compression is one of the most common loading modes in jaw, gyratory, and cone crushers, as well as in high-pressure grinding rolls, while impact loading is dominant in tumbling ball mills.

The test in common use and now industry-standard is the JK Drop Weight Test (JKDWT) [105, 106]. In the JKDWT, the energy required to break a rock under impact is estimated as the potential energy of the dropped weight, m_d (kg), from a given height, h (m). This energy is then normalized by the mass of the rock, m (kg), to give the specific energy, E_{CS} (kWh/t), as follows

$$E_{CS} = \frac{m_d g h}{3600 m}, \tag{27}$$

where g (9.81 m/s^2) is the gravitational acceleration. The degree of breakage is measured as the fraction of the original particle's mass that passes through an aperture of 1/10 of the original particle size after the impact event, referred to as the t_{10} of the progeny. The breakage test data are processed using Eq. (28) to establish the relationship between t_{10} and E_{CS},

$$t_{10} = A\left(1 - exp\left(-bE_{CS}\right)\right), \tag{28}$$

where A and b are parameters to be determined.

As discussed earlier, the energy required to fully break a rock, known as fracture energy, is defined as the area under the force–displacement curve. The ultrafast load cell (UFLC) is an enhanced drop weight test with instrumentation that allows for real-time measurements of fracture energy, particle strength, and stiffness [85, 107, 108]. It is important to note that what is referred to as fracture energy in the literature is often estimated as the area under the force–displacement curve up to the initial fracture event—the stored elastic energy needed to initiate breakage. This measure is also normalized by the mass of the rock to obtain the specific energy, a statistical measure that can be described by an upper-truncated lognormal probability distribution, which is available in Ansys Rocky DEM and Altair EDEM under the Tavares Breakage Model. For a more comprehensive review of single particle breakage tests, readers are referred to [106, 109, 110]. The aim here is to provide an overview of the data used as input in comminution modeling with DEM [9].

A rapid method for impact testing is the rotary impact tester [111], which was commercially adapted for ore testing in [112] as the JKRBT. Detailed investigations of single particle impacts can be conducted using air jet devices, where the samples are pneumatically accelerated and shot against a target [100, 113, 114]. In [100], a highly automated pneumatic cannon with integrated fragment analysis for rapid single particle testing is described.

The experiments mentioned above are integrated in DEM as follows: each particle is assigned an elastic energy threshold. If the energy absorbed by the particle during particle–particle or particle–plane contact exceeds this threshold, the particle will break; otherwise, it may undergo damage [108, 115]. Upon breakage, the particle is replaced by a collection of fragments or new particles, generated based on the t_{10} measure using the particle replacement method. Each fragment is then assigned a new energy threshold and inherits the kinematics of the parent particle. Overall, the particle replacement model (PRM), with the aforementioned calibration procedure, efficiently captures the product size distribution [91]. This efficiency arises from the fact that PRM does not consider the particle fragments throughout the DEM simulation, as in the bonded discrete element method, and the critical time step is proportional to the particle size [116].

3.2.3 Summary

In the particle replacement method, a rock can be treated as a single irregularly shaped particle that is replaced with smaller fragment particles if a failure criterion is met. This model representation enables the efficient capture of the product size distribution through calibration against single particle breakage tests. Additionally, it is computationally less expensive than the bonded discrete element method, which considers all the fragments throughout the entire simulation. However, the particle replacement method fails to accurately capture the force–displacement response of rock, especially when compared to the bonded discrete element method, and is less suitable for applications where flow behavior is of significant importance, such as conveying processes, as discussed in Sect. 3.2.

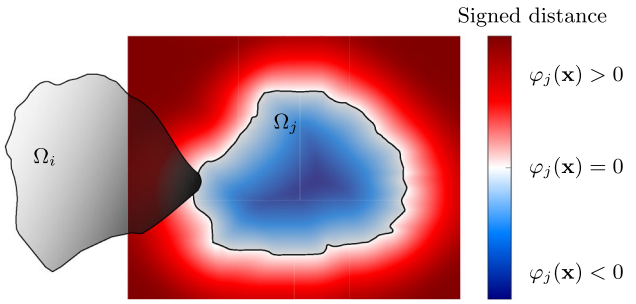

Fig. 14 Two-dimensional illustration of LS-DEM, showing the contact detection of grain Ω_i with grain Ω_j using the level-set function φ_j

3.3 Level-set discrete element method

A recent variant of DEM called the level-set discrete element method (LS-DEM) utilizes a discrete level-set function to model particles with arbitrary shapes in a particularly convenient manner [117]. An overview of this framework is presented in the context of breakage mechanics [118] and comminution.

3.3.1 Overview

Consider a particle indexed by j occupying a volume $\Omega_j \subset \mathbb{R}^3$. The cornerstone of LS-DEM is the definition of a level-set function $\varphi_j(\mathbf{x})$ that measures the signed distance from an arbitrary point $\mathbf{x}$ to the boundary of the particle Ω_j, denoted by $\partial\Omega_j$ and defined as the set of points where the level set function equals zero, i.e., $\partial\Omega_j = \{\mathbf{x} : \varphi_j(\mathbf{x}) = 0\}$ (see Fig. 14). On the other hand, if $\mathbf{x}$ is inside the particle, $\varphi_j(\mathbf{x})$ takes a negative value, while if $\mathbf{x}$ is outside the particle, $\varphi_j(\mathbf{x})$ is positive. The term "signed distance" thus refers to the fact that the distance is positive or negative depending on whether the point is outside or inside the particle.

As such, the level-set function characterizes the morphology of the particle as

$$\varphi_j(\mathbf{x}) = \begin{cases} -\inf_{y\in\partial\Omega_j} \|\mathbf{x}-\mathbf{y}\| \text{ if } \mathbf{x} \in \Omega_j, \\ +\inf_{y\in\partial\Omega_j} \|\mathbf{x}-\mathbf{y}\| \text{ if } \mathbf{x} \notin \Omega_j, \end{cases} \tag{29}$$

where $\|\mathbf{x}-\mathbf{y}\|$ denotes the Euclidian distance from $\mathbf{x}$ to a surface point $\mathbf{y}$. The inf operator represents the infimum or greatest lower bound, yielding the smallest possible distance between $\mathbf{x}$ and any point on the boundary.

This shape representation provides a seamless transition between experimental images and high-fidelity virtual avatars that preserve the shape, position, and orientation of every particle in a system [117]. Underscoring the crucial role of shape, this approach has allowed for accurate predictions of granular material behavior across the scales [119] and a broad range of interdisciplinary applications, e.g., [120–125].

Concerning computation, LS-DEM further provides a simple contact detection process based solely on evaluating a particle's level-set function at the surface coordinates of neighboring, potentially contacting objects (see Fig. 14). Once contact is detected, standard DEM operations are conducted to resolve the kinematics and kinetics, where the contact normal $\mathbf{n}_j^\alpha$ at a point $\mathbf{x}^\alpha$ is estimated based on the level-set gradient,

$$\mathbf{n}_j^\alpha = \frac{\nabla\varphi_j(\mathbf{x}^\alpha)}{\|\nabla\varphi_j(\mathbf{x}^\alpha)\|}\,. \tag{30}$$

A caveat of LS-DEM is the computational cost associated with discrete surface coordinates and level-set function values [126]. Recent works have shown that parallel implementations significantly alleviate this computational burden [126, 127]. Another point worth noting is that discretization convergence—i.e., insensitivity to the resolution of surface nodes and convergence to a physically meaningful solution as the node spacing decreases—was not guaranteed in the original version. However, recent works have resolved this issue [124, 128].

3.3.2 Extension to particle breakage

LS-DEM has been recently extended to account for particle breakage [118]. This approach has proven successful in capturing experimental observations in crushable sand, including the mechanical response, the evolution of particle size distribution and particle shape distribution [129], and the effects of cyclic loading [130]. Moreover, breakage-extended LS-DEM has enabled interdisciplinary applications such as sea ice melting and fracture [123].

Simple set operations are performed to induce fracture in LS-DEM particles, as illustrated in Fig. 15. In particular, a parent particle Ω_i with level-set function φ_i is allowed to break into two fragments, Ω_j and Ω_k, with level-set functions $\varphi_j = \max\{\varphi_i, \varphi_{\text{split}}\}$ and $\varphi_k = \max\{\varphi_i, -\varphi_{\text{split}}\}$, where φ_{split} is a splitting surface representing the crack path. This path is generally considered planar but other surfaces are also possible. Note that for each point $\mathbf{x}$, the function $\max\{\varphi, \vartheta\}$ gives the maximum value between $\varphi(\mathbf{x})$ and $\vartheta(\mathbf{x})$.

In principle, any breakage criterion may be employed to decide when and how a particle breaks. For instance, most studies have considered a stress-based criterion [118, 129, 130], e.g.,

$$\sigma_i^{\text{t}} \leq \sigma_i^{\text{cr}}, \tag{31}$$

where σ_i^{cr} is a critical stress parameter and $\sigma_i^{\text{t}} = \max\{\sigma_{i1}, \sigma_{i2}, \sigma_{i3}\}$ is the major principal stress in a particle Ω_i, computed from the average stress tensor over the particle volume $|\Omega_i|$,

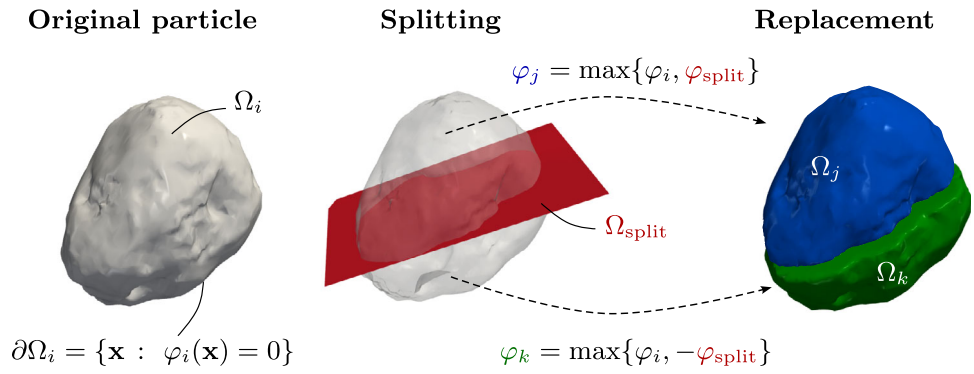

Fig. 15 Illustration of breakage in LS-DEM, showing the fracture of a particle Ω_i into fragments Ω_j and Ω_k along a plane Ω_{split}

$$\boldsymbol{\sigma}_i = \frac{1}{|\Omega_i|} \sum_{\alpha \in \mathrm{C}_i} \mathrm{sym}(\mathbf{F}_i^\alpha \otimes \mathbf{l}_i^\alpha). \tag{32}$$

Here, C_i is a set of contact indices with neighboring objects, $\mathbf{F}_i^\alpha$ is the contact force, and $\mathbf{l}_i^\alpha$ is the branch vector to the particle centroid.

The critical value σ_i^{cr}, as defined in [118], considers a size-dependent strength by recourse to Weibull's theory of brittle fracture. Consequently, for the initial particles in a system,

$$\sigma_i^{\mathrm{cr}} = \sigma_0^{\mathrm{cr}} \left[\left(\frac{d_0}{d_i} \right)^3 \ln(1 - P_{\mathrm{f}}) \right]^{1/m}, \tag{33}$$

where d_i is the particle's diameter, m is Weibull's modulus, and $P_{\mathrm{f}} \sim U(0, 1)$. The notation $P_{\mathrm{f}} \sim U(0, 1)$ means that the randomly generated failure probability P_{f} follows a uniform distribution over the interval [0, 1]. On the other hand, σ_0^{cr} is a reference stress corresponding to a reference grain diameter d_0 for which $P_{\mathrm{f}} = 1 - \mathrm{e}^{-1} \approx 0.63$, i.e., an approximately 63% failure probability. Once a parent particle Ω_i with strength σ_i^{cr} is set to fracture, the strength of a resulting fragment Ω_j is computed as

$$\sigma_j^{\mathrm{cr}} = \sigma_i^{\mathrm{cr}} \left(\frac{d_i}{d_j} \right)^{m/3}, \tag{34}$$

such that smaller fragment particles are stronger. On the other hand, the fragments inherit both the linear and angular velocities, and consequently the kinetic energy, of the parent particle.

An alternative modeling approach to particle breakage using LS-DEM involves particle bonding implemented with a brittle fracture criterion (Sect. 3.1.1), similar to the early work of Potyondy and Cundall [131].

3.3.3 Summary

The level-set discrete element method utilizes a discrete level-set function to describe particles of virtually any shape, including non-convex ones. It can enhance both the bonded discrete element method and the particle replacement method, allowing for a closer approximation of real rock shapes.

4 Future methodological developments

4.1 Particle replacement method

To summarize, a widely used approach in comminution modeling using DEM is the particle replacement method (Sect. 3.2), where a mother particle (most commonly spherical or superquadric, but could also be polyhedral) is replaced by various progeny particle shapes. While the particle size distribution and strength can be captured probabilistically through calibration using single particle breakage tests (Sect. 3.2.2), there are fundamental issues with this approach from a mechanistic perspective. Specifically, there is a lack of shape correspondence between the model particle and the real rock particle, despite consensus on the critical role of particle shape in the computational modeling of granular materials. Since both the loading condition and the mechanical response of the rock particle are shape-dependent, this relationship is lost when considering only the probability of fracture as a function of specific energy.

The level-set discrete element method (LS-DEM, Sect. 3.3) is of particular interest within this context because of its ability to capture the shape of virtually any rock. However, predicting the mechanical behavior of a rock using a single DEM particle is not a simple task, as the interaction between embedded rock grains plays a crucial role in capturing the nonlinear force–displacement response and the crack branching commonly observed in dynamic fracture. This can be addressed by splitting the particles, as presented in the breakage-enhanced LS-DEM framework discussed in Sect. 3.3.2 and the particle replacement method with Voronoi fragments in Sect. 3.2.1, or by introducing bonded particles into the mother particle based on either temporal or spatial constraints, which could enable more efficient use of compu-

tational resources compared to the bonded discrete element method.

Treating a rock before breakage as a single DEM particle in a virtual comminution machine is also a key advantage of the particle replacement method and LS-DEM, enabling timely results. Nevertheless, in applications where flow behavior is of interest (e.g., conveying processes), the kinetic energy transfer from the mother to progeny particles must be conserved. When generating smaller progeny particles with the same kinetic energy as the mother particle, as is often done for simplicity, the natural flow is distorted. Micromechanical DEM models of rock can facilitate the validation of such new measures, which will ultimately expand the range of applications of these replacement-based methods.

4.2 Bonded discrete element method

Alternatively, the Potyondy and Cundall bonded particle model of rock, along with variants that use polyhedral particle shapes and LS-DEM instead of spheres, is also applied in comminution modeling with DEM. However, this approach comes with increased computational overhead due to the need to explicitly model all bonded rock grains, compared to particle replacement methods. Advancements in GPU-based DEM and high-performance computing (HPC) have made it more feasible. Remaining challenges are associated with brittle fracture, where the sudden removal of bonds in the bonded particle model upon breakage leads to a mesh-dependent energy dissipation, which eventually approaches zero as the mesh is refined (Sect. 3.1.1). Therefore, a fracture energy regularization is needed to ensure accurate predictions independent of mesh size, as demonstrated through the cohesive zone model (Sect. 3.1.2) and the strong discontinuity approach (Sect. 3.1.3). While the strong discontinuity approach is widely used in lattice models of rocks, it can also be extended to DEM, as presented. This would allow for the use of coarser meshes, thus speeding up the simulation time.

The bond model must also account for loading rate dependency, as presented in Sect. 3.1.4. The current DEM-based comminution models are rate-independent and more suited to quasi-static load cases rather than the fast dynamic conditions observed in some comminution machines. As a result, these quasi-static models are likely to underpredict the forces applied to the equipment, which can affect not only force-response predictions but also the fragmentation behavior of rock, as discussed.

4.3 Calibration of material and contact parameters

Recent developments in [132–134] are focused on connecting geometallurgical data from geoblock models of the mine to the comminution machine response in the process. An important aspect here is the relationship between characterization experiments performed on drill core samples and how this data is used to calibrate DEM models. Calibration using Brazilian tensile strength tests and uniaxial compressive strength tests can be performed directly on drill core samples, providing a more direct rock mechanics-related response compared to traditional specific energy-based characterization tests on irregular particles or aggregated crushed drill core specimens (e.g., see [14]).

In this context, contact and bond material parameters must be determined. While there are experimental techniques to measure some of the contact material parameters (e.g., Young's modulus, coefficient of restitution, coefficient of friction, etc.), they are often used in combination with the so-called bulk calibration approach [135]. For example, parameters such as particle stiffness (Young's modulus), particle size, and density might be measured directly, while other parameters such as the coefficient of restitution or coefficient of friction might be determined using an inverse calibration process against field or laboratory experiments. The reasoning behind this hybrid approach is that the calibrated parameters compensate for the uncertainties associated with particle size and shape not being modeled accurately when large industrial systems are considered, or when the chosen contact model does not describe the contact mechanics well. For a comprehensive review of this topic, we refer the reader to [135]. When it comes to the bond material parameters (e.g., tensile and shear strength, the corresponding stiffness, and fracture energy), they are not typically directly measurable. Instead, DEM simulations of an experimental test such as a uniaxial compression test, Brazilian indirect tensile test, bending test, etc., are run; the stress–strain response and peak strength (as well as crack initiation and propagation) are observed, and the bond material parameters are adjusted iteratively until the simulation results match the experimental data [14, 29, 50, 136, 137]. However, rocks are heterogeneous materials; thus, once calibrated, it is important to assume an appropriate strength distribution function (e.g., Weibull, etc.) for the given material.

Furthermore, more accurately described representations of the mesh in relation to mineral lithology [138] open up opportunities for analyzing complex multi-component ore blends in comminution systems, and potentially even mineral liberation responses.

4.4 Applicability

Direct fracture modeling is often deemed computationally prohibitive in comminution. But this is slowly changing with the new computing capabilities. In a recent example [14], a bonded discrete element model with Voronoi cells was calibrated against a Brazilian disk test and compared with a detailed finite element model of rocks and digital image correlation (DIC) of the single particle breakage test of

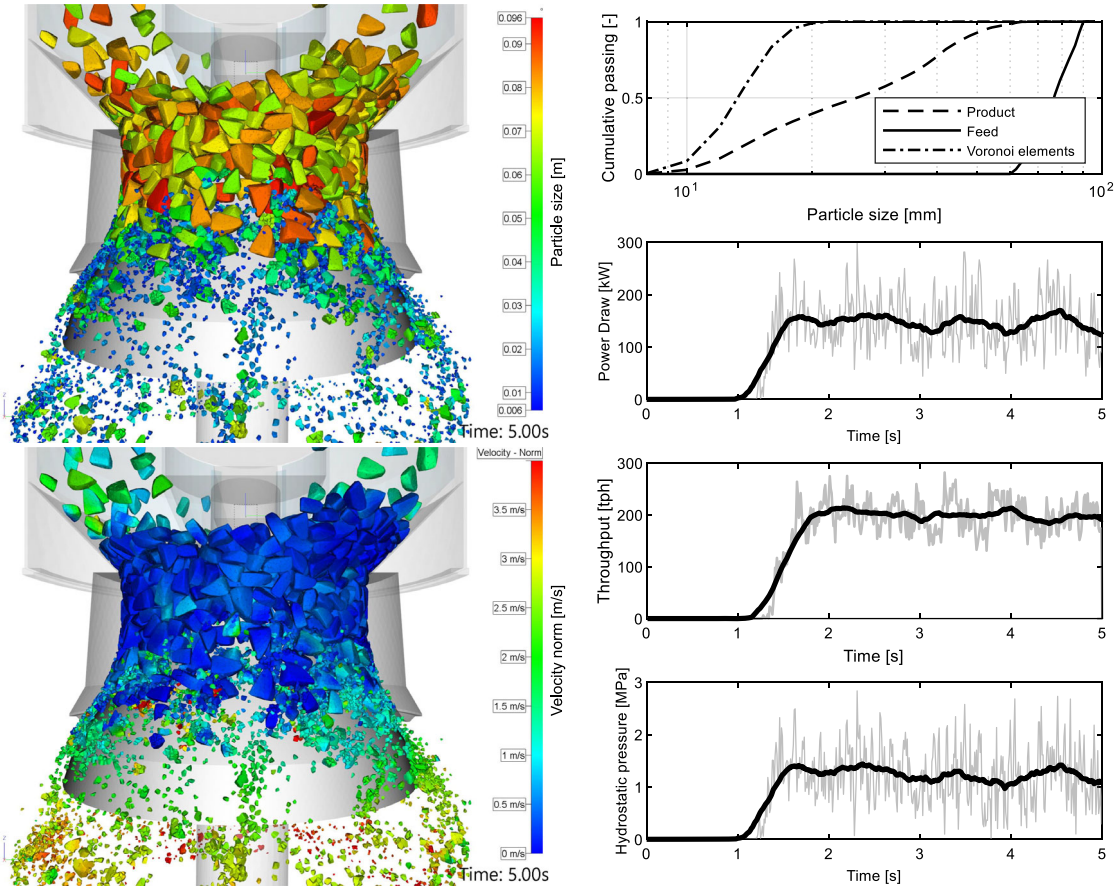

Fig. 16 Sandvik Hydrocone CH660 cone crusher simulation results, showing particles colored by size (top) and velocity (bottom), with machine responses on the right: size distributions, mass flow throughput, power draw, and hydrostatic pressure [14]

14 scanned rocks subjected to slow compression. The discrete element model predicted the crack pattern well but overestimated the force–displacement response. This overestimation was attributed to the coarse mesh used, which prevented the capture of crumbling (local contact damage) and thus the initially experimentally observed stiffening in the force–displacement response. The DEM approach was then demonstrated on a Sandvik Hydrocone CH660 cone crusher, with the feed and product size distributions shown in Fig. 16. The results of the demonstration simulation are presented in Fig. 16. The mean power draw is approximately 146 kW, the mean hydrostatic pressure is 1.22 MPa, and the throughput is 199 tons per hour (tph). The resulting nominal values for mass flow throughput, power draw, and hydrostatic pressure are of the right order of magnitude and are consistent with the typical expected values for that type of crusher model.

The computational performance, in terms of simulation time, was approximately 500 min per simulated second for the steady-state operation, using a time step of 2.5×10^{-7} s and 119,600 particle elements (each rock meshed with 198 Voronoi elements) active in the domain. The memory allocation on the GPU was approximately 3600 MB. A system with roughly six times the particle population could be simulated on the same graphics card if 24 GB of GPU memory were available. The simulation was performed on a workstation equipped with an Nvidia RTX 3090 graphics card and an AMD Ryzen 9 7950X 16-core processor. Therefore, these simulations are considered feasible from an industrial perspective, as useful results can be obtained overnight on a high-end workstation.

However, further work is needed to determine how many Voronoi elements are required to ensure that machine predictions are not sensitive to the meshing. The predicted product size distribution is particularly expected to depend on this. This is where the presented regularization techniques play a key role. Even though the methodological framework applies conceptually to the full crushing–grinding size range (mm – μm), the simulations themselves are demonstrated at scales computationally feasible for DEM (typically sub-mm scale), since direct simulation of micrometer-scale particles would require impractically small timesteps for industrial-scale processes. Ultimately, the current methods for rock fracture are designed to model high-resolution sub-domains of single

units (e.g., see Fig. 1), but they can be connected to other units to form a full circuit, as discussed in [15]. DEM cases can be packaged as a Functional Mockup Unit (FMU) and imported as an FMU block into third-party software such as MATLAB Simulink. This approach allows registration of input and output variables from the FMU, which can then interface with control modeling performed in Simulink.

Acknowledgements Vedad Tojaga and Johannes Quist would like to acknowledge the project 'Optimization of Crushing in Comminution of Mining Materials - OptiCrush', with the reference number 23-449, funded by the Åforsk Foundation, and the project 'eCoreX – AI-methods to Link Mineralogy and Core Sawing to Comminution Efficiency', with the diarienummer 2024-02683. Mijo Nikolić would like to acknowledge the project 'Parameter estimation framework for fracture propagation problems under extreme mechanical loads' (HRZZ-UIP-2020-02-6693), funded by the Croatian Science Foundation. Jacinto Ulloa would like to acknowledge support from the National Science Foundation, United States grant no. CBET-2526568.

Declarations

Conflict of interest On behalf of all authors, the corresponding author states that there is no Conflict of interest.

References

1. Aramendia E, Brockway PE, Taylor PG, Norman J (2023) Global energy consumption of the mineral mining industry: Exploring the historical perspective and future pathways to 2060. Glob Environ Chang 83:102745
2. Sandvik (2023) The future sandvik - rock processing solutions. https://www.youtube.com/watch?v=R0Y0GVX6jeo Accessed: 2025-05-06
3. Jeswiet J, Szekeres A (2016) Energy consumption in mining comminution. Procedia CIRP 48:140–145 (**The 23rd CIRP Conference on Life Cycle Engineering**)
4. Fuerstenau D, Abouzeid A-Z (2002) The energy efficiency of ball milling in comminution. Int J Miner Process 67(1):161–185
5. Lindqvist M (2008) Energy considerations in compressive and impact crushing of rock. Miner Eng 21(9):631–641
6. Quist J (2017) DEM modelling and simulation of cone crushers and high pressure grinding rolls. PhD thesis, Chalmers University of Technology, product and production development
7. Morrison R, Cleary P (2008) Towards a virtual comminution machine. Miner Eng 21(11):770–781 (**Discrete Element Methods (DEM) '07**)
8. Cundall PA, Strack OD (1979) A discrete numerical model for granular assemblies. Geotechnique, 29(1)
9. Weerasekara N, Powell M, Cleary P, Tavares L, Evertsson M, Morrison R, Quist J, Carvalho R (2013) The contribution of dem to the science of comminution. Powder Technol 248:3–24 (**Discrete Element Modelling**)
10. Bilock A (2020) A gpu polyhedral discrete element method - formulation and implementation of large scale simulations for non-spherical particles using novel gpu techniques. Master's thesis, Chalmers University of Technology - Department of Mathematical Sciences, Gothenburg, Sweden
11. Govender N, Wilke DN, Kok S, Els R (2014) Development of a convex polyhedral discrete element simulation framework for nvidia kepler based gpus. J Comput Appl Math 270, 386–400. Fourth international conference on finite element methods in engineering and sciences (FEMTEC 2013)
12. Govender N, Wilke DN, Wu C-Y, Khinast J, Pizette P, Xu W (2018) Hopper flow of irregularly shaped particles (non-convex polyhedra): Gpu-based dem simulation and experimental validation. Chem Eng Sci 188:34–51
13. Govender N, Wilke DN, Wu C-Y, Rajamani R, Khinast J, Glasser BJ (2018) Large-scale gpu based dem modeling of mixing using irregularly shaped particles. Adv Powder Technol 29(10):2476–2490
14. Suarez L, Tojaga V, Olsson E, Bilock A, Evertsson M, Kajberg J, Quist J (2025) Multiscale modeling of rock fracture in comminution – a comparative study of fem accuracy and dem scalability. Miner Eng 232:109488
15. Quist J, Edelvik E (2023) Advancing dynamic process modeling of comminution and classification circuits: a paradigm shift with gpu-enabled dem solver. in particles2023
16. Liang S, Feng Y, Wang Z (2025) Numerical methods and key issues for the study of particle material fragmentation behavior-a review. Powder Technol 451:120457
17. Koh EJ, Amini E, Gaur S, Becerra Maquieira M, Jara Heck C, McLachlan GJ, Beaton N (2022) An automated machine learning (automl) approach to regression models in minerals processing with case studies of developing industrial comminution and flotation models. Miner Eng 189:107886
18. Koh EJ, Amini E, McLachlan GJ, Beaton N (2021) Utilising a deep neural network as a surrogate model to approximate phenomenological models of a comminution circuit for faster simulations. Miner Eng 170:107026
19. Ghasemi Z, Neshat M, Aldrich C, Zanin M, Chen L (2025) Optimising sag mill throughput and circulating load using machine learning models: A multi-objective approach for identifying optimal process parameters. Miner Eng 232:109551
20. Munjiza A, Owen D, Bicanic N (1995) A combined finite-discrete element method in transient dynamics of fracturing solids. Eng Comput 12:145–174
21. Lei Z, Knight EE, Munjiza A, Rougier E (2024) Unified cohesive zone model (uczm) for fracturing and fragmenting solids. Eng Fract Mech 312:110598
22. Yan C, Zheng H (2017) Three-dimensional hydromechanical model of hydraulic fracturing with arbitrarily discrete fracture networks using finite-discrete element method. Int J Geomech 17. Published online: Nov 2, 2016
23. Yahya F, Hubert C, Leconte N, Dubar L (2024) A fem/dem adaptive remeshing strategy for brittle elastic failure initiation and propagation. Int J Numer Meth Eng 125(15):e7503
24. Voisin-Leprince M, Garcia-Suarez J, Anciaux G, Molinari J-F (2024) Two-scale concurrent simulations for crack propagation using fem-dem bridging coupling. Comput Particle Mech 11(5):2235–2243
25. Cornejo A, Mataix V, Zárate F, Oñate E (2020) Combination of an adaptive remeshing technique with a coupled fem-dem approach

for analysis of crack propagation problems. Comput Particle Mech 7(4):735–752
26. Rozmanov D, Kusalik PG (2010) Robust rotational-velocity-Verlet integration methods. Phys Rev E - Statistical, Nonlinear, Soft Matter Phys., 81(5)
27. Feng YT (2023) Thirty years of developments in contact modelling of non-spherical particles in dem: a selective review. Acta Mech Sin 39(1):722343
28. Lisjak A, Grasselli G (2014) A review of discrete modeling techniques for fracturing processes in discontinuous rock masses. J Rock Mech Geotech Eng 6(4):301–314
29. Potyondy D, Cundall P (2004) A bonded-particle model for rock. Int J Rock Mech Mining Sci 41(8):1329–1364 (**Rock Mechanics Results from the Underground Research Laboratory, Canada**)
30. Wessling A, Larsson S, Kajberg J (2024) A statistical bonded particle model study on the effects of rock heterogeneity and cement strength on dynamic rock fracture. Comput Particle Mech 11(3):1313–1327
31. Wu S, Wang G, Fan L, Guan W, Guo J, Liu Z, Wang Y (2024) A method to determine the bonded-particle model parameters for simulation of ores. Particuology 86:24–38
32. Quist J, Evertsson CM (2016) Cone crusher modelling and simulation using DEM. Miner Eng, 85
33. Jiang C, Gou D, Li C, Wu G, An X, Wang J, Guo P (2023) Crushing characteristics and performance evaluation of iron ore in a cone crusher: a numerical study. Miner Eng 204:108429
34. Quan J, Rong G, Xu L, Chen Z (2023) A three-dimensional grain-based model for studying the microscopic fracture behaviour of granite. Comput Geotech 159:105427
35. Wessling A, Larsson S, Jonsén P, Kajberg J (2022) A statistical DEM approach for modelling heterogeneous brittle materials. Comput Particle Mech 9(4)
36. Zhang Y, Wong LNY, Chan KK (2019) An extended grain-based model accounting for microstructures in rock deformation. J Geophys Res Solid Earth 124(1):125–148
37. Potapov AV, Campbell CS (1994) Computer simulation of impact-induced particle breakage. Powder Technol 81(3):207–216
38. Orozco LF, Delenne J-Y, Sornay P, Radjai F (2019) Discrete-element model for dynamic fracture of a single particle. Int J Solids Struct 166:47–56
39. Cantor D, Azéma E, Sornay P, Radjai F (2017) Three-dimensional bonded-cell model for grain fragmentation. Comput Particle Mech 4:441–450
40. Wang T, Liu HZ, Xiao ML, Zhuo L, Xie HQ, He JD (2023) Improvement of size effect simulation based on an energy-balanced exponential softening bond model and fracture energy regularization. Comput Struct 280
41. Tian Y, Weijermars R, Zhou F, Hu L, Liu T, Liu H (2023) Advances in stress-strain constitutive models for rock failure: review and new dynamic constitutive failure (dcf) model using core data from the tarim basin (china). Earth Sci Rev 243:104473
42. Govender N, Wilke DN, Kok S (2016) Blaze-demgpu: modular high performance dem framework for the gpu architecture. SoftwareX 5:62–66
43. Liu G-Y, Xu W-J, Sun Q-C, Govender N (2020) Study on the particle breakage of ballast based on a gpu accelerated discrete element method. Geosci Front 11(2):461–471 (**Grain Crushing in Geoscience Materials**)
44. Liu G-Y, Xu W-J, Govender N, Wilke DN (2021) Simulation of rock fracture process based on gpu-accelerated discrete element method. Powder Technol 377:640–656
45. Ibrahimbegovic A (2006) Nonlinear solid mechanics: theoretical formulations and finite element solution methods, vol. 1 of solid mechanics and its applications. Dordrecht: Springer Dordrecht, 1 ed., 2009. Original French edition published by Hermes Science – Lavoisier, Paris
46. Ma G, Zhou W, Chang X-L (2014) Modeling the particle breakage of rockfill materials with the cohesive crack model. Comput Geotech 61:132–143
47. Liu L, Ji S (2019) Bond and fracture model in dilated polyhedral dem and its application to simulate breakage of brittle materials. Granular Matter 21:41
48. Li X, Kuang J, Jiang S, Ji S (2024) Bonded particle model for dilated polyhedron considering fracture modes and its application to lateral resistance of ballast bed in cold regions. Powder Technol 439
49. Ibrahimbegovic A, Delaplace A (2003) "Microscale and mesoscale discrete models for dynamic fracture of structures built of brittle material. Comput Struct 81(12)
50. Nguyen NH, Bui HH, Nguyen GD, Kodikara J (2017) A cohesive damage-plasticity model for DEM and its application for numerical investigation of soft rock fracture properties. Int J Plasticity 98
51. Simo JC, Oliver J, Armero F (1993) An analysis of strong discontinuities induced by strain-softening in rate-independent inelastic solids. Comput Mech 12:277–296
52. Pham BH, Brancherie D, Davenne L, Ibrahimbegovic A (2013) Stress-resultant models for ultimate load design of reinforced concrete frames and multi-scale parameter estimates. Comput Mech 51:347–360
53. Tojaga V, Kulachenko A, Östlund S, Gasser TC (2023) Hybrid of monolithic and staggered solution techniques for the computational analysis of fracture, assessed on fibrous network mechanics. Comput Mech 71:39–54
54. Tojaga V, Kulachenko A, Östlund S, Gasser TC (2021) Modeling multi-fracturing fibers in fiber networks using elastoplastic Timoshenko beam finite elements with embedded strong discontinuities — Formulation and staggered algorithm. Comput Methods Appl Mech Eng 384
55. Čarija J, Nikolić M, Ibrahimbegovic A, Nikolić Ž (2020) Discrete softening-damage model for fracture process representation with embedded strong discontinuities. Eng Fract Mech 236:107211
56. Zhang QB, Zhao J (2014) A review of dynamic experimental techniques and mechanical behaviour of rock materials. Rock Mech Rock Eng 47(4):1411–1478
57. Semsari Parapari P, Parian M, Rosenkranz J (2020) Breakage process of mineral processing comminution machines - an approach to liberation. Adv Powder Technol 31(9):3669–3685
58. Saksala T, Jabareen M (2019) Numerical modeling of rock failure under dynamic loading with polygonal elements. Int J Numer Anal Meth Geomech 43(12):2056–2074
59. Wang WM, Sluys LJ, de Borst R (1997) Viscoplasticity for instabilities due to strain softening and strain-rate softening. Int J Numer Meth Eng 40(20):3839–3864
60. Saksala T, Brancherie D, Harari I, Ibrahimbegovic A (2015) Combined continuum damage-embedded discontinuity model for explicit dynamic fracture analyses of quasi-brittle materials. Int J Numer Meth Eng 101(3):230–250
61. Zubelewicz A, Bažant ZP (1987) Interface element modeling of fracture in aggregate composites. J Eng Mech 113(11)
62. Bažant ZP, Tabbara MR, Kazemi MT, Pijaudier-Cabot G (1990) Random Particle Model for Fracture of Aggregate or Fiber Composites. J Eng Mech 116(8)
63. Nikolić M, Karavelić E, Ibrahimbegovic A, Miščević P (2018) Lattice element models and their peculiarities. Arch Comput Methods Eng 25(3):753–784
64. Cusatis G, Pelessone D, Mencarelli A (2011) Lattice discrete particle model (LDPM) for failure behavior of concrete. I: Theory. Cement Concrete Composites, 33

65. Grassl P, Jirásek M (2010) Meso-scale approach to modelling the fracture process zone of concrete subjected to uniaxial tension. Int J Solids Struct 47(7):957–968
66. Schlangen E, van Mier J (1992) Simple lattice model for numerical simulation of fracture of concrete materials and structures. Mater Struct 25:534–542
67. Rasmussen LL, de Farias MM (2019) Lattice modelling of gravity and stress-driven failures of rock tunnels. Comput Geotech 116:103183
68. Nikolic M, Ibrahimbegovic A, Miscevic P (2015) Brittle and ductile failure of rocks: embedded discontinuity approach for representing mode i and mode ii failure mechanisms. Int J Numer Meth Eng 102(8):1507–1526
69. Nikolić M, Do XN, Ibrahimbegovic A, Nikolić Željana (2018) Crack propagation in dynamics by embedded strong discontinuity approach: enhanced solid versus discrete lattice model. Comput Methods Appl Mech Eng 340:480–499
70. Nikolic M, Ibrahimbegovic A (2015) Rock mechanics model capable of representing initial heterogeneities and full set of 3D failure mechanisms. Comput Methods Appl Mech Eng 290:209–227
71. Tojaga V, Gasser TC, Kulachenko A, Östlund S, Ibrahimbegovic A (2023) Geometrically exact beam theory with embedded strong discontinuities for the modeling of failure in structures. Part I: Formulation and finite element implementation. Comput Methods Appl Mech Eng 410
72. Ljukovac S, Ibrahimbegovic A, Mejia-Nava R-A, Imamovic I (2024) Geometrically exact 3d beam theory with embedded strong discontinuities for modeling of localized failure in bending. Int J Solids Struct 297:112850
73. Zhang K, Yan H, Lu J-M, Ren B (2024) Rod-bonded discrete element method. Graph Models 133:101218
74. Cleary PW (2001) Recent advances in dem modelling of tumbling mills. Miner Eng 14(10):1295–1319
75. Cleary P (2001) Modelling comminution devices using dem. Int J Numer Anal Meth Geomech 25(1):83–105
76. Åström JA, Herrmann HJ (1998) Fragmentation of grains in a two-dimensional packing. Eur Phys J B 5(3):551–554
77. Barrios GK, Jiménez-Herrera N, Tavares LM (2020) Simulation of particle bed breakage by slow compression and impact using a dem particle replacement model. Adv Powder Technol 31(7):2749–2758
78. Brzeziński K, Gladky A (2022) Clump breakage algorithm for dem simulation of crushable aggregates. Tribol Int 173:107661
79. Cleary PW, Sinnott MD (2015) Simulation of particle flows and breakage in crushers using dem: part 1 - compression crushers. Miner Eng 74:178–197
80. Li H, McDowell G, Lowndes I (2014) Discrete element modelling of a rock cone crusher. Powder Technol 263:151–158
81. Tavares LM, Rodriguez VA, Sousani M, Padros CB, Ooi JY (2021) An effective sphere-based model for breakage simulation in dem. Powder Technol 392:473–488
82. Delaney GW, Morrison RD, Sinnott MD, Cummins S, Cleary PW (2015) Dem modelling of non-spherical particle breakage and flow in an industrial scale cone crusher. Miner Eng 74:112–122
83. de Arruda Tino AA, Tavares LM (2022) Simulating breakage tests using the discrete element method with polyhedral particles. Comput Particle Mech 9(4):811–823
84. Tavares LM, André FP, Potapov A, Maliska C (2020) Adapting a breakage model to discrete elements using polyhedral particles. Powder Technol 362:208–220
85. Tavares LM, King RP (1998) Single-particle fracture under impact loading. Int J Mineral Proc 54(1)
86. Rocky DEM Inc. (2018) Tavares breakage model in rocky dem
87. Flavio A, Potapov A, Tavares LM (2019) Simulation of single particle breakage using non-round particles in rocky dem. 26th Int Mining Congress Mining Exhibition Turkey
88. Zhou W, Wang D, Ma G, Cao X, Hu C, Wu W (2020) Discrete element modeling of particle breakage considering different fragment replacement modes. Powder Technol 360:312–323
89. Barrios GK, Tavares LM (2016) A preliminary model of high pressure roll grinding using the discrete element method and multi-body dynamics coupling. Int J Miner Process 156:32–42
90. Rodriguez VA, Barrios GKP, Bueno G, Tavares LM (2021) Investigation of lateral confinement, roller aspect ratio and wear condition on hpgr performance using dem-mbd-prm simulations. Minerals 11(8):801
91. Jiménez-Herrera N, Barrios GK, Tavares LM (2018) Comparison of breakage models in dem in simulating impact on particle beds. Adv Powder Technol 29(3):692–706
92. Tavares LM, das Chagas AS (2021) A stochastic particle replacement strategy for simulating breakage in dem. Powder Technol 377:222–232
93. Sousani M, Chagas A, Saxena A, Yang Y (2019) Simulation of surface damage and body breakage by using dem. 2019 NAFEMS World Congress in Quebec Canada
94. Tavares LM (2022) Review and further validation of a practical single-particle breakage model. Kona Powder Part J 39:62–83
95. Denzel M, Prenner M, Sifferlinger NA, Antretter T (2023) A breakage model for DEM based on a probabilistic particle replacement with Voronoi fragments. Miner Eng 203
96. Denzel M (2023) A breakage model for discrete element simulations applied to iron ore sinter. Phd thesis, University of Leoben, Leoben
97. Denzel M, Prenner M, Sifferlinger NA (2022) A probabilistic particle replacement model to simulate bulk material degradation during conveying processes using dem: Montanuniversität leoben. Proceedings MHCL 2022 - 24th international conference on material handling, constructions and logistics in Belgrad, Serbia, 29–36
98. Denzel M (2022) Partikelbruch in der fördertechnik - prüfmethodik und simulation mittels diskrete elemente methode (particle breakage during conveying processes - test method and simulation with the discrete element method). In 10. Kolloquium - Fördertechnik im Bergbau (O. Langefeld, ed.), (Clausthal-Zellerfeld), pp. 89–101, Papierflieger Verlag GmbH
99. Denzel M (2022) Partikelbruch in der fördertechnik: Prüfmethodik und simulation mittels diskrete elemente methode. Bergbau - Zeitschrift für Rohstoffgewinnung Energie Umwelt 73(10):436–440
100. Denzel M, Prenner M, Sifferlinger NA (2022) Development of an automated single particle impact tester for iron ore sinter. Miner Eng 175:107291
101. Denzel M, Prenner M (2022) Partikelbruchvorhersage an einem dynamischen übergabesystem und vergleich mit einer herkömmlichen schurre mittels dem (particle breakage prediction on a dynamic transfer system and comparison with a conventional chute using dem). BHM Berg- Huettenmaenn Monatsh 167(2):66–75
102. Denzel M, Prenner M, Sifferlinger NA (2023) Solid state material driven turbine to reduce segregation during bunker filling. BHM Berg- und Hüttenmännische Monatshefte
103. Prenner M, Denzel M, Sifferlinger NA (2023) Cross flow turbine to reduce size segregation effects in storage processes. ICBMH 2023 - 14th international conference on bulk materials storage, handling and transportation
104. Denzel M, Prenner M, Sifferlinger NA (2024) Evaluation of mixing effects and particle breakage on a cross flow turbine with dem. BHM Berg- Huettenmaenn Monatsh 169(4):211–220

105. Napier-Munn TJ, Morrell S, Morrison RD, Kojovic T (1996) Mineral comminution circuits: their operation and optimisation. Julius Kruttschnitt Mineral Research Centre The University of Queensland
106. Yahyaei M, Hilden M, Shi F, Liu LX, Ballantyne G, Palaniandy S (2016) Comminution, pp. 157–199. Cham: Springer International Publishing
107. King RP, Bourgeois F (1993) Measurement of fracture energy during single-particle fracture. Miner Eng 6(4)
108. Tavares LM, King RP (2002) Modeling of particle fracture by repeated impacts using continuum damage mechanics. Powder Technol 123(2-3)
109. Tavares LM (2007) Chapter 1 breakage of single particles: Quasi-static," in Particle Breakage (Salman AD, Ghadiri M, Hounslow MJ eds.), vol. 12 of Handbook of Powder Technology, pp. 3–68, Elsevier Science B.V
110. Mwanga A, Rosenkranz J, Lamberg P (2015) Testing of ore comminution behavior in the geometallurgical context—A review. Minerals 5(2)
111. Schönert K, Markstscheffel M (1986) Liberation of composite particles by single particle compression, shear and impact loading. Proceedings of the 6th European Symposium Comminution
112. Shi F, Kojovic T, Larbi-Bram S, Manlapig E (2009) Development of a rapid particle breakage characterisation device - the jkrbt. Miner Eng 22(7–8):602–612
113. Meier M, John E, Wieckhusen D, Wirth W, Peukert W (2008) Characterization of the grinding behaviour in a single particle impact device: studies on pharmaceutical powders. Eur J Pharmaceutical Sci Off J Eur Federation Pharmaceutical Sci 34(1):45–55
114. Cavalcanti PP, Petit HA, Thomazini AD, de Carvalho RM, Tavares LM (2021) Modeling of degradation by impact of individual iron ore pellets. Powder Technol 378:795–807
115. Cleary PW, Delaney GW, Sinnott MD, Cummins SJ, Morrison RD (2020) Advanced comminution modelling: Part 1 - crushers. Appl Math Model 88:238–265
116. Burns SJ, Piiroinen PT, Hanley KJ (2019) Critical time step for DEM simulations of dynamic systems using a Hertzian contact model, Int J Numerical Methods Eng 119(5)
117. Kawamoto R, Andò E, Viggiani G, Andrade JE (2016) Level set discrete element method for three-dimensional computations with triaxial case study. J Mech Phys Solids 91
118. Harmon JM, Arthur D, Andrade JE (2020) Level set splitting in DEM for modeling breakage mechanics. Comput Methods Appl Mech Eng 365
119. Kawamoto R, Andò E, Viggiani G, Andrade JE (2018) All you need is shape: predicting shear banding in sand with LS-DEM. J Mech Phys Solids 111:375–392
120. Buarque de Macedo R, Andò E, Joy S, Viggiani G, Pal RK, Parker J, Andrade JE (2021) Unearthing real-time 3d ant tunneling mechanics. Proc Natl Acad Sci 118(36):e2102267118
121. Wang Y, Li L, Hofmann D, Andrade JE, Daraio C (2021) Structured fabrics with tunable mechanical properties. Nature 596(7871):238–243
122. Zhou Z, Andreini M, Sironi L, Lestuzzi P, Andò E, Dubois F, Bolognini D, Dacarro F, Andrade JE (2023) Discrete structural systems modeling: benchmarking of LS-DEM and LMGC90 with seismic experiments. J Eng Mech 149(12):04023097
123. Moncada R, Gupta M, Thompson A, Andrade JE (2023) Level set discrete element method for modeling sea ice floes. Comput Methods Appl Mech Eng 406:115891
124. Feldfogel S, Karapiperis K, Andrade JE, Kammer DS (2024) A discretization-convergent level-set-discrete-element-method using a continuum-based contact formulation. Int J Numer Meth Eng 125(5):e7400
125. Zhou Z, Moncada R, Jones N, Ulloa J, Fu X, Andrade JE (2024) Simplified level set discrete element modeling of particle suspension flows in microfluidics: clogging statistics controlled by particle friction and shape. Granular Matter 26(2):39
126. Duriez J, Bonelli S (2021) Precision and computational costs of level set-discrete element method (LS-DEM) with respect to DEM. Comput Geotechnics 134
127. Tan P, Sitar N (2024) Parallel implementation of LS-DEM with hybrid MPI+OpenMP. Comput Geotech 172
128. van der Haven DL, Fragkopoulos IS, Elliott JA (2023) A physically consistent Discrete Element Method for arbitrary shapes using Volume-interacting Level Sets. Comput Methods Appl Mech Eng 414
129. Harmon JM, Seo D, Buscarnera G, Andrade JE (2022) Insight into contact forces in crushable sand using experiments and predictive particle-scale modelling. Géotechnique 74(3):238–249
130. Ulloa J, Zhou Z, Harmon J, Andrade JE (2024) Cyclic-loading effects in sand: a micromechanical study considering particle breakage. Granular Matter 26
131. Harmon JM, Karapiperis K, Li L, Moreland S, Andrade JE (2021) Modeling connected granular media: particle bonding within the level set discrete element method. Comput Methods Appl Mech Eng 373:113486
132. Houshmand N, Esmaeili K, Goodfellow S, Carlos Ordóñez-Calderón J (2023) Predicting rock hardness using gaussian weighted moving average filter on borehole data and machine learning. Miner Eng 204:108448
133. Bhuiyan MM (2021) Establishing geometallurgical relationships between rock comminution behaviour and rapid and portable drill core-scale rock characterization tests. Ph.d. thesis, Department of Civil and Mineral Engineering, University of Toronto
134. Lieberwirth H, Duriagina A, Klichowicz M (2025) Quantifying the impact of mineral microstructure on the comminution of ores and rocks. In Proceedings of Comminution '25, (Cape Town, South Africa)
135. Coetzee C (2017) Review: calibration of the discrete element method. Powder Technol 310:104–142
136. Oñate E, Zárate F, Miquel J, Santasusana M, Celigueta MA, Arrufat F, Gandikota R, Valiullin K, Ring L (2015) A local constitutive model for the discrete element method. Application to geomaterials and concrete. Comput Particle Mech 2(2):139–160
137. Scholtès L, Donzé F-V (2013) A dem model for soft and hard rocks: role of grain interlocking on strength. J Mech Phys Solids 61(2):352–369
138. Klichowicz M, Lieberwirth H (2021) Grain-based dem for particle bed comminution. Minerals 11(3)